Nanoscale

PAPER

View Article Online
View Journal | View Issue



Cite this: *Nanoscale*, 2024, **16**, 16227

# Multi-responsive poly-catecholamine nanomembranes†

Adam Krysztofik, [a] Marta Warżajtis,[a] Mikołaj Pochylski, [a] Marcel Boecker, [b] Jiyao Yu, [b] Tommaso Marchesi D'Alvise,[b] Przemysław Puła, [c] Paweł W. Majewski, [c] Christopher V. Synatschke, [b] Tanja Weil [b] and Bartlomiej Graczykowski *[a]

The contraction of nanomaterials triggered by stimuli can be harnessed for micro- and nanoscale energy harvesting, sensing, and artificial muscles toward manipulation and directional motion. The search for these materials is dictated by optimizing several factors, such as stimulus type, conversion efficiency, kinetics and dynamics, mechanical strength, compatibility with other materials, production cost and environmental impact. Here, we report the results of studies on bio-inspired nanomembranes made of poly-catecholamines such as polydopamine, polynorepinephrine, and polydextrodopa. Our findings reveal robust mechanical features and remarkable multi-responsive properties of these materials. In particular, their immediate contraction can be triggered globally by atmospheric moisture reduction and temperature rise and locally by laser or white light irradiation. For each scenario, the process is fully reversible, *i.e.*, membranes spontaneously expand upon removing the stimulus. Our results unveil the universal multi-responsive nature of the considered polycatecholamine membranes, albeit with distinct differences in their mechanical features and response times to light stimulus. We attribute the light-triggered contraction to photothermal heating, leading to water desorption and subsequent contraction of the membranes. The combination of multi-responsiveness, mechanical robustness, remote control *via* light, low-cost and large-scale fabrication, biocompatibility, and low-environment impact makes polycatecholamine materials promising candidates for advancing technologies.

Received 12th March 2024,
Accepted 29th May 2024

DOI: 10.1039/d4nr01050g

rsc.li/nanoscale



## Introduction

Multi-responsive polymeric materials represent one of the most exciting and vividly emerging research fields stimulating technological advancement.[1–3] Scientific efforts have focused on materials exhibiting reversible changes in their properties when exposed to various stimuli, including temperature, pH, light, electric and magnetic fields, vapor, or moisture. Such polymers offer many functionalities, opening new avenues for high-end applications. Hitherto, the ongoing advances have led to the development of self-cleaning surfaces,[4] smart windows,[5] rewritable optical displays,[6] bioresponsive drug nanocarriers in gene therapy,[7,8] blood-contacting devices,[9] MRI contrast agents,[10] self-regulated insulin delivery and glucose sensing systems,[11] and thermally adjustable multicolor indicators.[12]

Another important application of smart polymers concerns their ability to transform the energy of external stimuli into mechanical work to develop synthetic muscles and soft robots.[13–16] Temperature changes primarily trigger their actuation, leading to macroscopic deformations through thermally induced cleavage of the additional cross-links.[2] However, heat-based actuation lacks control and accuracy, and the response time is high. This has led to the emergence of photo-active actuators that respond to light, offering the benefits of remote and precise control with spatiotemporal resolution.[2,3] Light as a stimulus allows for non-contact actuation, making these materials suitable for soft robotics and sensing system applications, with the potential for miniaturization and automation. The actuators typically utilize light-activated molecular transformations (crystalline–isotropic phase transition,[17] *cis–trans* isomerization,[18] ring-opening,[19] bond exchange,[20] cycloadditions,[21] transesterification[22]) to achieve various deformations and motions. However, these mechanisms only

[a]*Faculty of Physics, Adam Mickiewicz University, Uniwersytetu Poznańskiego 2, 61-614 Poznań, Poland. E-mail: bartlomiej.graczykowski@amu.edu.pl*
[b]*Max Planck Institute for Polymer Research, Ackermannweg 10, 55128 Mainz, Germany*
[c]*Faculty of Chemistry, University of Warsaw, Pasteur 1, 02-093 Warsaw, Poland*

†Electronic supplementary information (ESI) available: Structural and elastic properties of poly-catecholamine pristine membranes. Moisture response of the polydopamine film PDA 200c transferred onto a silicon substrate. Photoactuation dynamics of poly-catecholamine membranes irradiated with a red laser. Photoactuation dynamics of polydopamine membranes irradiated with white light. Brillouin light scattering results. Cyclic voltammograms of polycatecholamine films. See DOI: https://doi.org/10.1039/d4nr01050g

provide relatively slow macroscopic actuation (1 s timescales[17,22]) and require an annealing step to ensure reversibility.[23,24] Thus, photo-chemical actuation often requires the control of two separate triggers.

On the other hand, photothermally driven motion due to thermal expansion, phase transition, or molecule sorption benefits from manipulating deformation by a single stimulus. In particular, a porous polymer serving as a guest medium for absorbents can exhibit significant volume changes and perform rapid and reversible movements by using light as a heating factor that initiates the release of molecules. In addition to the well-established water-adsorbing poly-*N*-isopropylacrylamide (PNIPAM),[25] polydopamine (PDA)[9,26,27] reveals stimulus-responsiveness,[28] remarkable adhesive properties,[29–32] catalytic activity,[8,33–37] versatility for functionalization,[38] and biocompatibility, which make it attractive for biomedicine.[39–43] Moreover, PDA exhibits exceptional photothermal characteristics across the full range of the visible spectrum,[44] akin to closely related analogs in the melanin family,[45,46] and maintains its structural integrity even at temperatures of up to 130 °C.[47] The potential practical applications include humidity sensors,[48] small-scale robots,[49] molecular sieves,[50] phototransistors,[51] photonic crystals,[52] selective ion transport for electrochemical energy conversion and storage,[53] membrane separators in redox flow batteries,[54] water desalination,[55] oil/water separation,[56] photocatalytic nanocomposites for energy production,[34] hydrogen production,[57] and separation layers in solar cells.[58] Recently, other related monomers such as tyrosine, phenylalanine, epinephrine, or phenylethylamine have been polymerized by oxidation reactions[59] similar to PDA formation. These polymers reveal distinct properties, indicating the great potential of catechol-based polymers for various applications. However, their responsiveness to stimuli leading to actuation has not yet been reported.

In this work, we utilize time-dependent optical reflectance, X-ray reflectometry (XRR), and micro-Brillouin light scattering (μ-BLS) to investigate the mechanical response and material properties such as mass density and Young modulus of ultrathin (~20 nm thick) polycatecholamine (PCA) membranes exposed to various external stimuli. In particular, we study two PDA nanomembranes that differ in fabrication conditions and two nanomembranes made of polynorepinephrine (PNE) and polydextrodopa (PdDOPA). We demonstrate that the contraction of these nanomembranes can be triggered by light (coherent and white), temperature increase, and humidity reduction. Their ability to perform mechanical motion appears to be a universal feature. However, their contraction/relaxation times and mechanical properties differ depending on the monomer and the polymerization conditions.

## Results and discussion

We fabricated PCA using the electrochemical deposition method through cyclic voltammetry as reported previously by us.[28,60,61] The films were polymerized at room temperature (RT) on gold-coated microscope slides from a solution of the target monomer dissolved in phosphate buffer. Three different monomers were used (Fig. 1a): dopamine, dextrodopa (3,4-dihydroxyphenylalanine), and norepinephrine to deposit films of polydopamine (PDA), polydextrodopa (PdDOPA), and polynorepinephrine (PNE), respectively. The fabrication procedure is schematically illustrated in Fig. 1b, while further details can be found in the Methods section. The potential varied linearly at a scan rate of 10 mV $s^{-1}$ for 15 cycles for PDA 15c, PdDOPA, and PNE. A higher scan rate of 200 mV $s^{-1}$ was used for 200 cycles for a polydopamine sample denoted herein as PDA 200c for a comparison with PDA 15c. After the deposition, the films were immersed in a carbonate buffer to increase the cross-linking density. We performed an electrochemical removal procedure to detach the films from the gold surface. Then, the films were mechanically stripped off using a sacrificial film of polyvinyl alcohol (PVA) and transferred onto the water surface. The floating nanomembranes were then scooped using a 1 μm-thick holey $Si_3N_4$ support and, in this way, suspended over a grid of circular holes with the diameter ranging from 20 to 100 μm. Additionally, the PCAs from the same fabrication process were transferred onto Si wafer chips for XRR characterization. Finally, the transferred PCA membranes were further immersed in water to dissolve any residual PVA and dried under ambient room conditions. Fig. 1c and d show the optical images of an exemplary PDA membrane and film deposited on a custom-made $Si_3N_4$ grid and Si wafer chip.

To evaluate mechanical features such as the Young modulus ($E$), flexural rigidity ($D$), and residual stress ($\sigma_0$) of the membranes, we applied μ-BLS spectroscopy.[28] Using this contactless technique, we probed GHz thermally populated fundamental antisymmetric Lamb waves/phonons (flexural waves) whose frequency ($f$) at long wavelengths ($\lambda$) is governed by the dispersion relationship:[62,63]

$$f = \frac{q}{2\pi}\sqrt{\frac{d^2}{12\rho}\frac{E}{1-\nu^2}q^2 + \frac{\sigma_0}{\rho}} \quad (1)$$

where $q = 2\pi/\lambda$ is the wavenumber and $\nu = 0.3$ is the Poisson ratio.[60] To determine thicknesses ($d$) and mass densities ($\rho$), we utilized XRR and examined the reference films deposited on Si-wafer chips. The values obtained at RT and relative humidity RH = 30% are listed in Table S1 (ESI†). Overall, the average thicknesses were in the range of 17–28 nm. The mass densities of both PDA samples were very similar and generally much higher than those of classical polymers such as polystyrene (PS), polypropylene, or polymethyl methacrylate (PMMA), to name a few.[64] Notably, PNE and PdDOPA were lighter than PDA, with the latter having a much lower mass density than water under the same ambient conditions.

The results of μ-BLS experiments (Fig. S4, ESI†) are gathered in Table S1 (ESI†) and Fig. 1e. For PDA 15c, PDA 200c, and PNE membranes, we obtained $E$ = 8.1 GPa, 11.0 GPa, and 16.3 GPa, respectively, which are in good agreement with the data found in the literature (6–18 GPa).[60,63] Overall, these

 

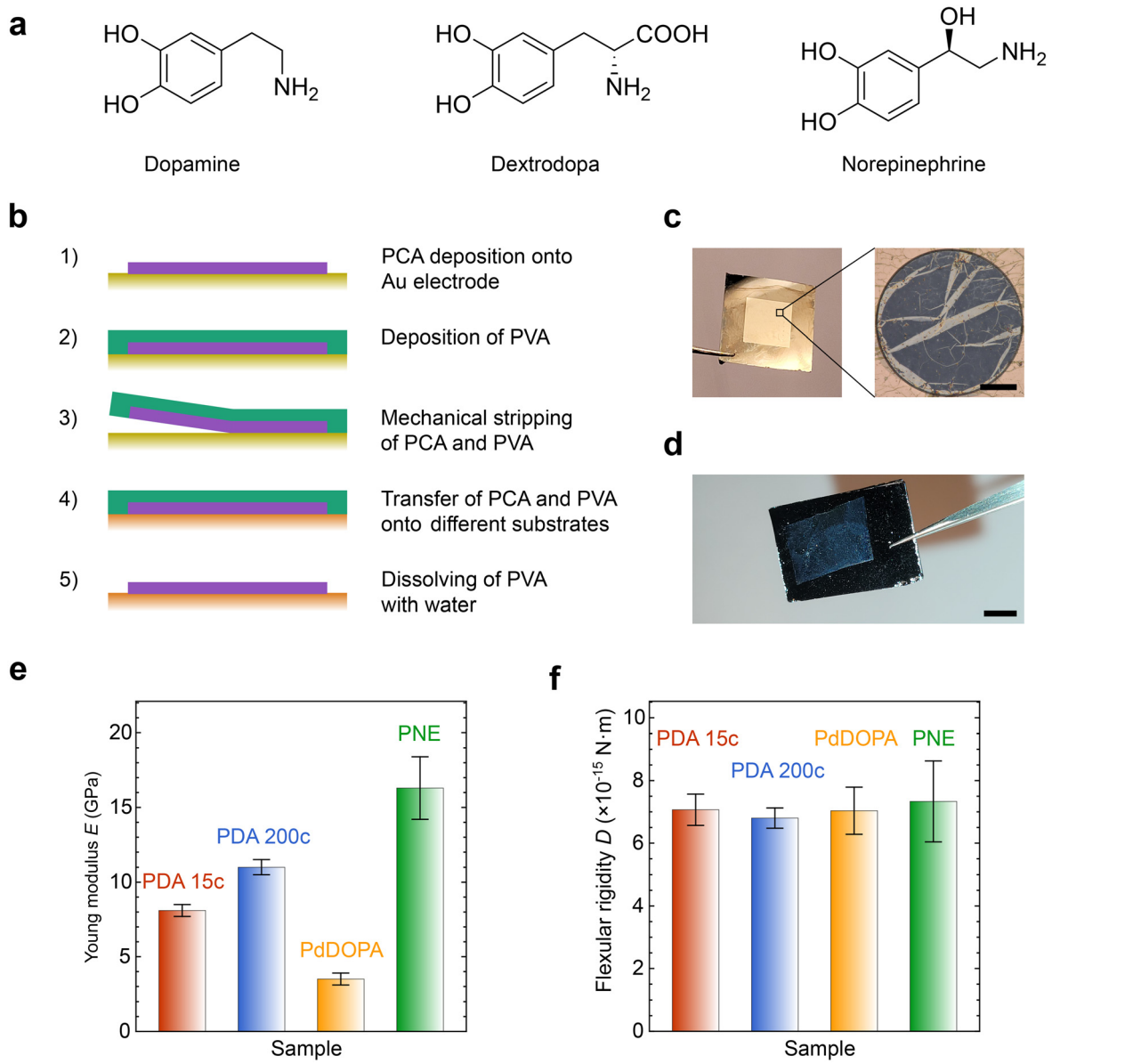


**Fig. 1** (a) Chemical structures of the monomers used to obtain membranes and films of PDA, PdDOPA, and PNE. (b) Schematic procedure of sample fabrication; the main steps are: (1) electropolymerization of the PCA film, (2) deposition of a sacrificial PVA layer, (3) mechanical stripping of PVA together with the PCA film, (4) transfer of the bilayer onto a different substrate, (5) dissolving of the PVA layer in water to obtain PCA on the chosen substrate. (c) Exemplary photo of the $Si_3N_4$ grid covered with PDA and optical image of a freestanding membrane. The scale bar is 20 μm. (d) Exemplary photo of the PDA film (brighter, parallelogram-like region) transferred onto a silicon substrate. The scale bar is 5 mm. (e) Comparison of the Young moduli determined for the PCA membranes under ambient room conditions. (f) Comparison of the flexular rigidity $D$ determined for the PCA membranes at 23 °C and RH = 30%.

values are much higher than those of standard polymers such as PS or PMMA.[65–68] Furthermore, it corroborates the substantial mechanical resilience of the membranes, which, despite a diameter-to-thickness ratio of about 4000, can withstand free suspension without breaking. On the other hand, the Young modulus of the PdDOPA membrane was approximately three times smaller ($E$ = 3.5 GPa) compared to those of PDA and PNE membranes, which is consistent with its lower stability and durability (Fig. 2–4). This finding corresponds with the apparent tearing observed in optical images of PdDOPA suspended over holes with a diameter of 80 μm (Fig. 2–4). For PdDOPA, we only observed membranes fully intact when suspended over 20 μm holes. Following eqn (1), we determined a non-zero residual tensile stress $\sigma_0$ from the μ-BLS data of all the considered samples ranging from 0.5 to 19.5 MPa. These values are relatively small when compared to the intrinsic elasticity of the membranes, albeit they are sufficient to make the as-fabricated membranes flat. Based on the determined material properties, we evaluated the flexural rigidity ($D$) of the membranes:[69]

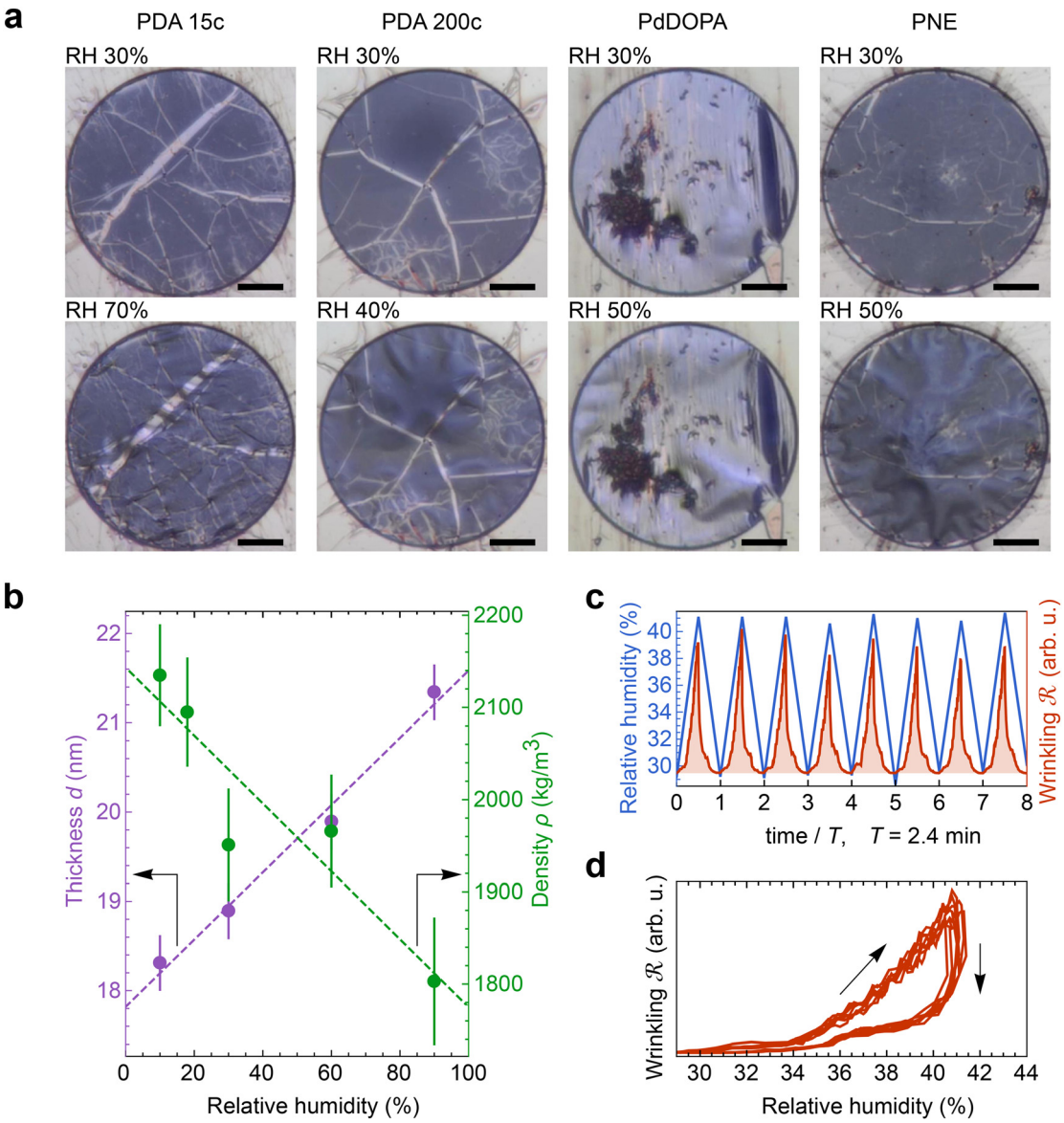


**Fig. 2** Response of the PCA membranes to moisture. (a) Optical images of the membranes taken at a relative humidity (RH) of 30% (upper panel) and increased humidity (lower panel). The black scale bar is 20 μm. (b) One-dimensional swelling of the PDA 200c film transferred onto a silicon substrate evidenced by thickness and density dependence on the relative humidity. (c and d) Cyclic testing of the freestanding PDA 200c membrane response to moisture. In (c), relative humidity and wrinkling parameters as a function of time are shown, while panel (d) displays the dependency of the wrinkling parameter $\mathcal{R}$ on the relative humidity.

$$D = \frac{Ed^3}{12(1-\nu^2)} \tag{2}$$

It is worth noting that the values of $D$, which reflect the ability to resist bending deformation, are comparable among the membranes. As we can conclude from Fig. 1f, the variations in the Young modulus between PDA, PNE, and PdDOPA are counterbalanced by differences in their thickness, resulting in similar values of $D \cong 7 \times 10^{-15}$ N m.

Fig. 2a (top panel) shows optical images of four as-fabricated membranes made of PDA (15c and 200c), PdDOPA, and PNE at RT and a relative humidity (RH) of 30%. The pristine membranes are flat with a minor contribution of three-folded parts visible as brighter flaws. The increase in RH of the atmosphere at RT results in their wrinkling, as displayed in the bottom panel of Fig. 2a. This phenomenon is observed in all the studied samples and results from swelling and, thereby, expansion of the membranes due to the water sorption from the atmosphere. Generally, the extent of the observed wrinkling depends on the residual stress, *i.e.*, the visible deformation starts at a different RH.

To provide a more quantitative picture of the humidity-induced expansion of the membranes, we conducted XRR measurements of the PDA film transferred onto a silicon sub-

 

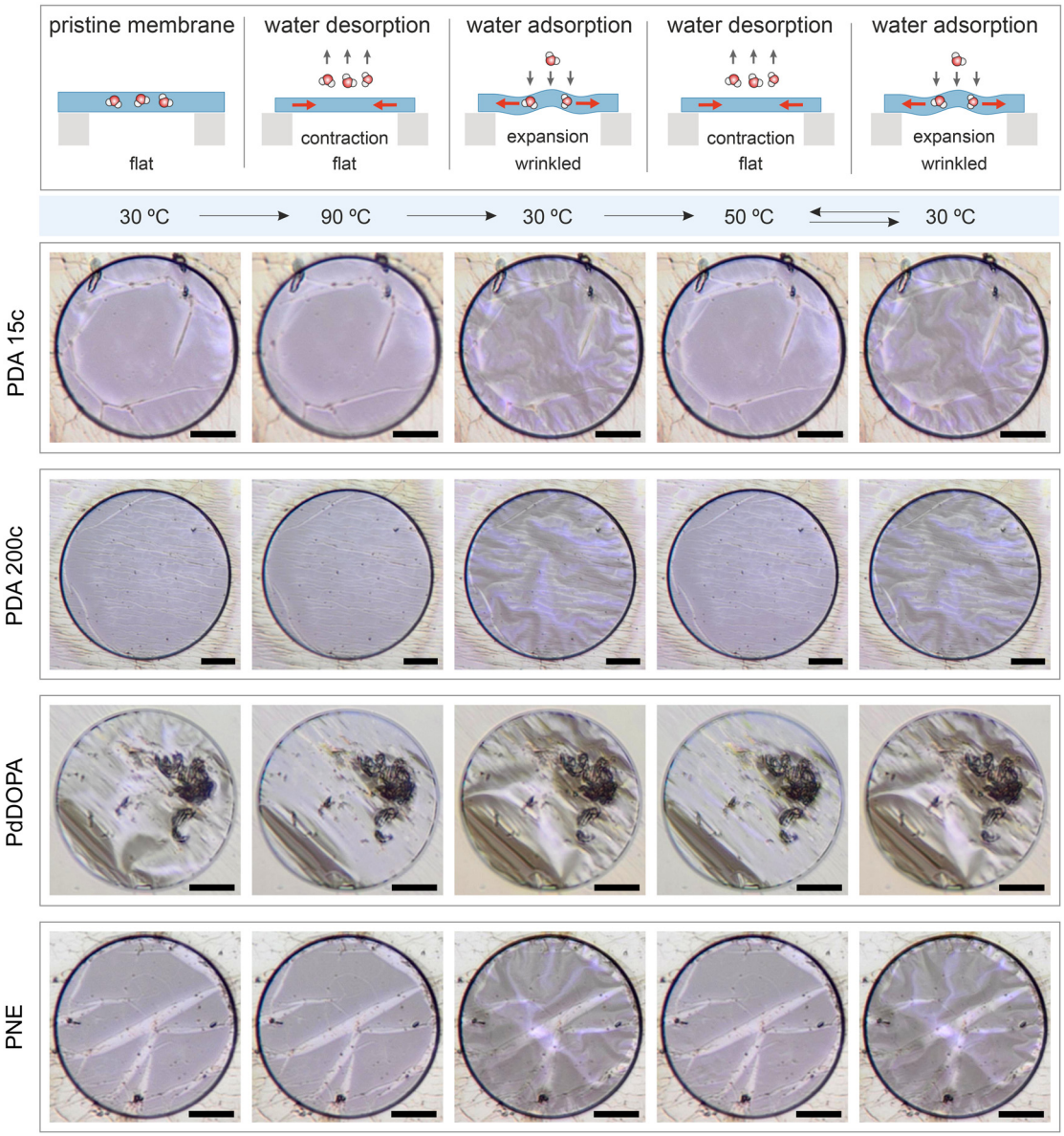


**Fig. 3** Response of the PCA membranes to a uniform thermal stimulus. The left column schematically shows consecutive experiment steps (denoted with black dashed arrows) and a response of the cross-sectioned membrane subjected to global heating. The optical images of the PDA 15c, PDA 200c, PdDOPA, and PNE membranes display their morphology under the selected environmental conditions. The black scale bar is 20 μm.

strate, examining changes in thickness and density as a function of RH at RT (Fig. S1, ESI†). As shown in Fig. 2b, with an increase in RH from 10% to 90%, the film thickness linearly increases by about 17% of the initial value, while the mass density decreases by about 14%. These findings confirm that the PDA swelling results from the adsorption of water molecules. In the case of the freestanding membrane, water adsorption leads to expansion in three dimensions. Thus, in the first step, it releases the residual stress and, finally, leads to buckling and wrinkling of the membrane.

Wrinkling of the membranes due to increased RH is a reversible process that can be concluded at first glance from optical imaging. We performed an optical microscopy image analysis of the PDA 200c membrane to understand this behavior better. Fig. 2c illustrates the cyclic changes in RH and the corresponding membrane response over time described herein, with a wrinkling factor $\mathcal{R}$. The quantity $\mathcal{R}$ is defined as the variance of contrast in a differential image taken with respect to the one at RH 30% (ESI Videos 1 and 2†). High values of $\mathcal{R}$ indicate a wrinkled membrane, while low values signify a flat membrane. Within one cycle, RH was increased from 30% to 50% and then decreased to 30% with a rate of about 8.3% $min^{-1}$, lasting for 8 cycles, which is denoted by the solid line in Fig. 2c. Notably, the membrane response given by $\mathcal{R}$ is delayed with respect to the stimulus for all the cycles as the RH linearly starts rising from 30%. This behavior is even

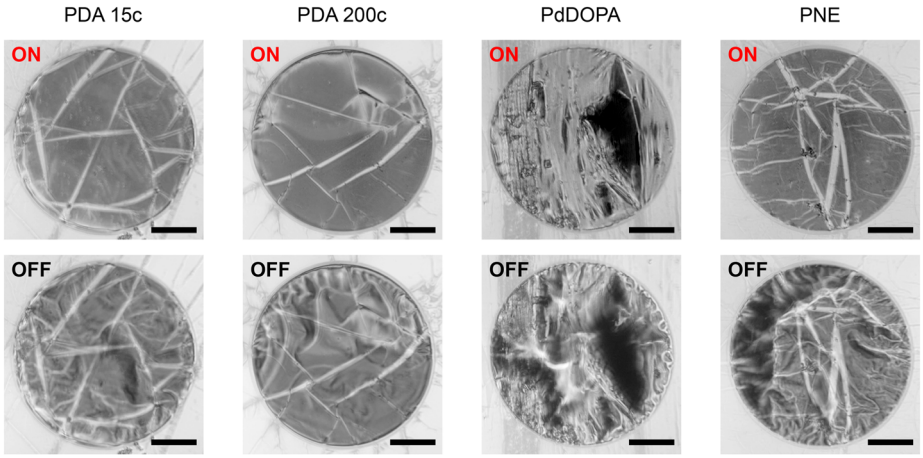


**Fig. 4** (a) Optical images of the various PCA membranes subjected to the red laser light of 20 mW (ON) and the dark conditions (OFF). The black scale bar is 20 μm. To record the photos, a set of polarizers and an optical filter were used to cut off red laser illumination.

more evident in Fig. 2d, depicting $\mathcal{R}$ *vs.* RH, and can be explained by the expansion accommodated mainly by the residual stress up to about RH = 34%. Subsequently, as the membrane starts buckling and wrinkling, $\mathcal{R}$ linearly follows the increase of RH. When RH starts decreasing, we observe a sudden drop in $\mathcal{R}$, followed by its almost negligible decrease ranging from RH = 34% to 30%. The latter trend reflects a gradual increase of the in-plane stress while the membrane remains flat. As we can notice from Fig. 2d, the membrane wrinkling takes two different paths under cyclic increase and decrease of RH. Notably, in this quasi-static experiment, the membrane contraction, triggered by the release of water molecules, is more rapid than the expansion. Nevertheless, this hysteresis can be explained by the non-equilibrium nature of buckling and local stress accommodation and release within the wrinkled membrane rather than the non-reciprocal sorption of water. The analysis encompassing differential images also allowed us to pinpoint membrane areas prone to wrinkling. Based on that, we have not identified any distinct patterns or features common to the studied samples. Therefore, we conclude that each membrane's wrinkling motif is unique, arising from residual stress, thickness variations, and imperfections (folds and cracks) induced during membrane deposition onto the hole grid.

A global or local thermal stimulus at constant ambient RH can alter the moisture level and, thereby, the membranes' mechanical state. Notably, the initial state of all considered as-fabricated membranes, which is flat under ambient room conditions, can be permanently altered by global heating. This effect is illustrated in Fig. 3. When uniformly heated to 90 °C, residual water molecules in the membrane are released, causing the polymer to contract. The resulting thermally induced in-plane stress (in addition to the residual stress) can be accommodated over time through lateral shrinkage of the whole film that is not firmly attached to the supporting $Si_3N_4$ substrate. As the temperature decreases to 30 °C, the membranes absorb moisture from the surrounding atmosphere, expand, and become permanently wrinkled. Subsequent heating and cooling cycles have the same effect on the mechanical state of the membrane (flat *vs.* wrinkled). It is worth noting that an increase in temperature by 20 °C (from 30 °C) is sufficient to flatten all the studied membranes from their wrinkled state fully.

Control over the mechanical state of individual membranes can also be achieved through local photoinduced (photothermal) heating (ESI Videos 3–6†). The underlying physical mechanism of membrane wrinkling remains consistent with the uniform annealing method described above. However, in this case, light irradiation is limited to the membrane area, as the spot of the red laser (660 nm) approximately matches the membrane diameter. The transition from a flat to a deformed state is already observed at a laser power of 10 mW. Subsequent power rise to 20 mW does not induce further deformation, and the membrane reaches a stable operational state. We estimate that applying 20 mW of the laser power raises the membrane temperature from 24 °C to approximately 70 °C.[28] Therefore, the applied laser power corresponds to temperatures well below the point of polymer decomposition (400 °C)[47] and below 125 °C, at which membrane damage was observed.

Optical images in Fig. 4 depict substantial morphological changes in the membranes when exposed to red laser light heating (660 nm) after the initial pre-treatment described above. Under dark conditions, the membranes appear wrinkled, but when illuminated, they flatten due to the heat-induced water release and polymer contraction. Utilizing a low-power probe green laser beam (<1 m W, 532 nm) to record the reflectivity signal from the membrane surface offers additional means for the real-time observation of membrane morphology (Fig. 5a). The intensity of the signal varies significantly depending on the state of the membrane. During the laser illumination (ON state), the probe beam reflectivity is high due to the specular reflection of the beam from the membrane surface, whereas under dark conditions (OFF state), it is

 

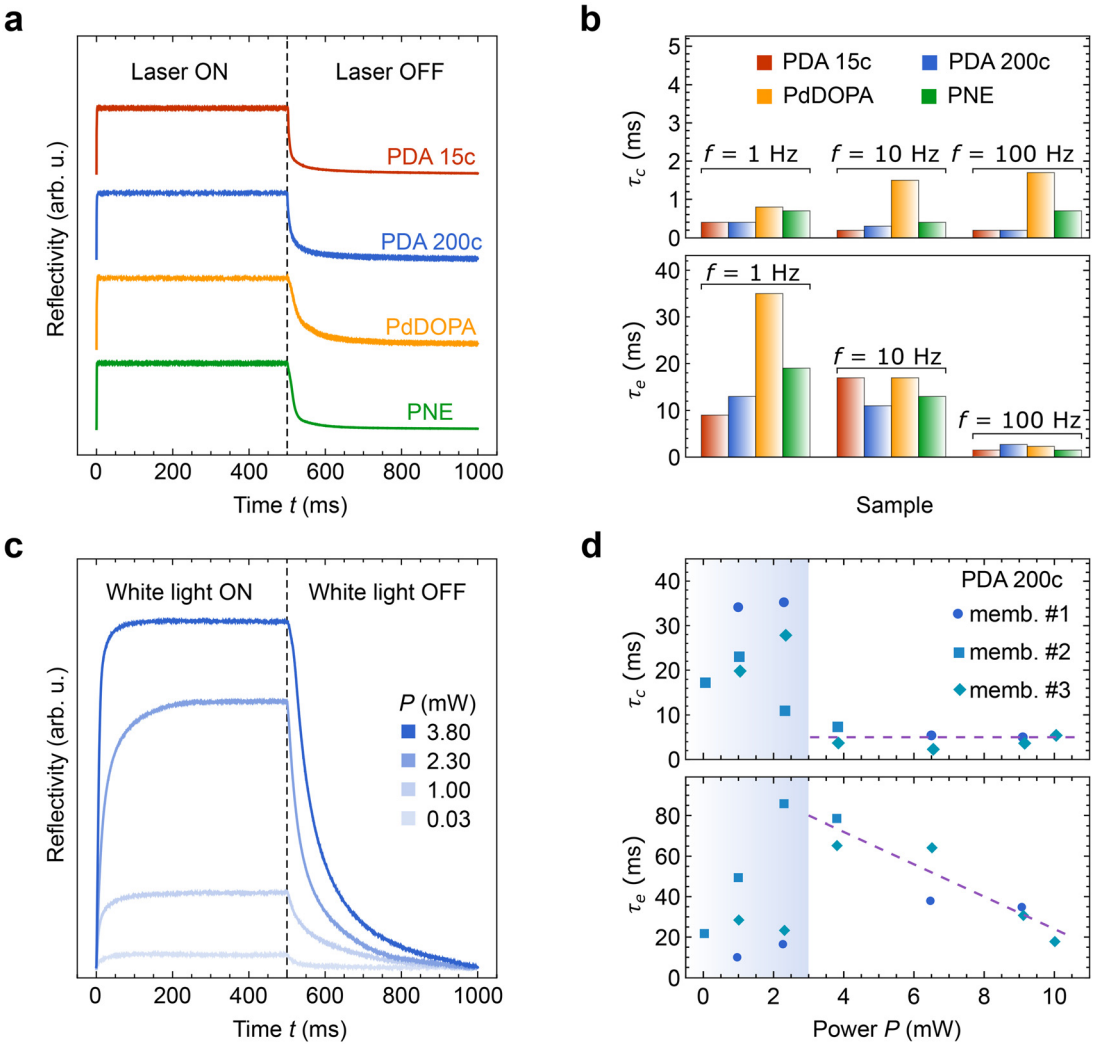


**Fig. 5** (a) Photoactuation dynamics of PCA membranes irradiated with a red laser at a repetition rate of 1 Hz and power $P$ = 40 mW. (b) Comparison of the contraction $\tau_c$ and expansion $\tau_e$ times for the membranes stimulated with the red laser at a repetition rate of 1, 10, and 100 Hz and $P$ = 40 mW. (c) The reflectivity of the PDA 200c membrane stimulated with white light at a repetition rate of 1 Hz and different powers ($P$). (d) Comparison of the contraction and expansion times for the PDA 200c membranes subjected to white light stimulus at different powers ($P$) and a repetition rate of 1 Hz. Symbols #1–#3 denote different membranes of the same PDA 200c sample. The shaded area displays the low-power region. Dashed lines serve as a guide to the eye.

low as the probe light is diffusively reflected. The heating laser light intensity can be modulated over time, whereas the membrane response can be quantified by the reflected light collected by the photodiode detector. This time-dependent reflectivity measurement also enables the investigation of membrane motion with a high temporal resolution, enabling the determination of the contraction time $\tau_c$ (as the reflectivity signal rises to $1 - 1/e$ of its amplitude) and the expansion time $\tau_e$ (as the signal amplitude drops to $1/e$).

The membranes respond to the heating laser stimulus occurring on a subsecond timescale, enabling their photoactuation within a frequency range of 1 to 100 Hz (Fig. 5a). For all the studied membranes, $\tau_c$ remains below 1 ms at a repetition rate of 1 Hz. The rapid contraction of the membrane can be attributed to the nearly instantaneous rise in temperature and water desorption induced by laser heating. In contrast, the expansion times ($\tau_e$) are noticeably longer, which can be explained by the spontaneous nature of this process. Under dark conditions, heat dissipation governs the water adsorption rate *via* conduction and convection mechanisms that are significantly slower than abrupt laser heating. Consequently, for PDA and PNE membranes, $\tau_e$ ranges from 9 to 19 ms at $f$ = 1 Hz. However, for PdDOPA, $\tau_e$ is even further increased to 35 ms. This slower response can hardly be attributed to the elastic features of the membrane. As mentioned, the flexural rigidity is nearly the same for all studied PCA membranes, although the Young modulus noticeably varies. The greater thickness of the PdDOPA membrane (28 nm) compared to those of PDA and PNE (17–21 nm) may be one reason contributing to its slower relaxation owing to reduced water

diffusion. Another factor that we can tentatively point out is a subtle interplay between porosity, degree of crosslinking, and the molecular dynamics of hydroxyindole segments.[28] Nevertheless, these elevated $\tau_e$ values do not hinder clear photoactuation at frequencies of 10 and 100 Hz for all studied samples (Fig. S2, ESI†). At higher frequencies, $\tau_c$ remains below 1 ms for PDA and PNE and 2 ms for PdDOPA as shown in Fig. 5b. Interestingly, $\tau_e$ gradually decreases with increasing stimulant frequency, reaching 3 ms at $f$ = 100 Hz for all PCA membranes. This shows superior responsiveness of PCA membranes to the coherent light stimulus compared to PDA-based heterogeneous photoactuators operating at about 1 s timescales.[17,22,70]

In addition to monochromatic light, the photoactuation of the membranes can be driven by white light at power levels as low as a few milliwatts (Fig. 5c and Fig. S3 in ESI†). Irradiation with a broad-spectrum LED yields qualitatively similar responses to those of red laser light, even within the range of $P$ = 0.03–3.8 mW (Fig. 5c). At power levels below 3 mW, $\tau_c$ and $\tau_e$ vary between 10 and 90 ms, as marked with the shaded region in Fig. 5d. This observation suggests that water contained within the membranes is only partially released during light irradiation. At light powers higher than 3 mW, the contraction times remain relatively constant (approximately 5 ms), while the expansion times moderately decrease from 80 to 20 ms as the power increases from 3 to 10 mW. Therefore, water sorption efficiency is characterized by a threshold power of 3 mW, above which photoactuation becomes increasingly effective. We anticipate that within the following power increase above 10 mW, both $\tau_c$ and $\tau_e$ will closely match the values determined with red laser irradiation (estimated at $P$ = 40 mW), although it requires a further experimental study and the use of a stronger white light source or multiple LEDs.

## Conclusions

In summary, the fabricated PCA nanomembranes exhibit remarkable mechanical flexibility, ease of integration with diverse surfaces, and responsiveness to multiple stimuli, including humidity, temperature, and light. The underlying mechanism driving the motion of these membranes relies on the reversible sorption of water. Specifically, our study reveals that the silicon-integrated PDA film undergoes one-dimensional swelling when the relative humidity increases from 10% to 90%, resulting in a 17% increase in film thickness and a 14% decrease in density from the initial value. Consequently, the muscle-like contractions observed in the freestanding membranes are a universal characteristic shared among PDA, PdDOPA, and PNE. Notably, we have demonstrated remote, sub-second photoactuation triggered by coherent irradiation and broad-spectrum white light, inducing heating through the photothermal effect. The observed photoactuation has been registered across laser repetition frequencies ranging from 1 Hz to 100 Hz. The rapid response primarily stems from the small thickness of the membranes, allowing for swift desorption of water molecules under light exposure and efficient water resorption under dark conditions. The determined contraction and expansion times are of the order of milliseconds and tens of milliseconds, respectively, significantly shorter than reported photoactuation times for materials such as ~1 mm-thick PDA-coated liquid crystal elastomers (100 ms),[17] ~150 μm-thick liquid crystalline elastomers doped with PDA nanoparticles (15 s),[22] 0.6 mm-thick PNIPAM with a spiropyran moiety (~15 min),[71] and 12 μm-thick azobenzene-doped nematic liquid-crystal polymers (~2–4 s).[72] Moreover, we have shown that the state of our as-fabricated (flat) membranes can be permanently modified through global thermal heating as well as local photoinduced heating, giving us complete control over individual membrane morphology. Among the studied catecholamines, PDA and PNE emerge as the most promising materials for practical applications due to their high elasticity and robust Young modulus values of ~8–16 GPa. While PdDOPA membranes exhibit indistinguishable flexural rigidity from PDA and PNE, the significantly smaller Young modulus of 3.5 GPa and observed membrane tearing categorize PCA as a more demanding material for future development.

The robust multi-sensitivity of PCA, together with its ease of integration onto any surface, paves a unique path for future applications. Electropolymerized membranes represent versatile components for designing micro- and nanodevices. Their excellent adhesion to diverse surfaces, relatively high elasticity, and wide photothermal capacity make them valuable for wireless actuation with high spatiotemporal resolution tasks. Furthermore, our study brings us closer to the low-cost development of on-chip integrated moisture and light sensors and photoresponsive actuators. Finally, we anticipate that our research will inspire further exploration into PCA-based hybrid heterostructures, the chiral properties of these membranes investigated with circularly polarized light, a deeper understanding of the molecular behavior of water dynamics within membranes, and an evaluation of their long-term aging.

## Methods

### Film preparation

Electropolymerization was done by cyclic voltammetry using a Metrohm Autolab potentiostat (AUTOLAB PGSTAT 204) with a standard three-electrode setup. A gold-covered glass slide was used as a working electrode, a gold wire as a counter electrode, and an Ag/AgCl (3 M KCl) as a reference electrode. All reactions were performed in a 35 mL electrochemical cell (Metrohm) at room temperature and in air.[60]

After cleaning the gold slides in an argon plasma (0.2 mbar) for 10 minutes, they were immersed in a 1 mg $mL^{-1}$ solution of the respective monomer (dopamine hydrochloride, D/L-norepinephrine hydrochloride or 3,4-dihydroxy-D-phenylalanine) in a phosphate buffer. Phosphate buffer (pH 7, 100 mM) was prepared using sodium phosphate dibasic anhydrous (99%) and sodium phosphate monobasic (99%) (Sigma-Aldrich) in MilliQ water.[61] The potential was cycled from 0.5 V

 

to −0.5 V with a scan rate of 10 mV $s^{-1}$ for 15 cycles for PDA 15c, PNE, and PdDOPA or with a scan rate of 0.2 V $s^{-1}$ for 200 cycles for PDA 200c. The films were rinsed with MilliQ water and dried under a nitrogen flow.

### Film transfer onto holey $Si_3N_4$ membranes and Si wafers

Carbonate buffer (pH 10, 100 mM) was prepared using sodium bicarbonate (>99.7%) and sodium carbonate (>99.8%) from Sigma-Aldrich, in MilliQ water.[28,61] The films were immersed in the carbonate buffer for 30 minutes. Afterward, they were rinsed with MilliQ water and dried under a nitrogen flow. The same three-electrode setup as for the film preparation was used with the film on the gold slide as a working electrode to perform an electrochemical removal cycle. Therefore, the potential was swept between 1.2 V and −0.8 V for 3 cycles with a scan rate of 20 mV $s^{-1}$. The films were rinsed with MilliQ water and dried under a nitrogen flow before distributing 200 μL of a PVA solution (10 wt%) onto the film and partially on the gold slide. Polyvinyl alcohol (PVA) 80% hydrolyzed 9–10 kDa MW (Sigma-Aldrich) was used to prepare the 10 wt% solutions in Milli-Q water.[28] PVA was cured in an oven (40 °C) for 30 minutes. The film and the sacrificial PVA layer were mechanically removed from the gold slide and transferred. One batch of films was transferred onto the water surface. The floating films were scooped using 1 μm-thick holey $Si_3N_4$ membranes and, in this way, suspended over a grid of circular holes with the diameter ranging from 20 to 100 μm. The other batch of films was transferred onto Si wafers. All samples were dried overnight at room temperature, and to remove the remaining PVA, the samples were again immersed in MilliQ water for 3 h and dried again for 3 h.

### Optical microscopy

Optical imaging was performed on an Olympus BX53 microscope, supplied with Linkam THMS600 temperature and RHGen humidity controllers, enabling observations of the membranes at temperatures ranging from 30 to 90 °C and relative humidities from 30% up to 70%.

### Optodynamic measurements

The dynamical response of the membranes triggered by the light stimulus was investigated with a home-built optical setup.[28] To induce the periodical photoactuation, a linearly polarized red laser (660 nm) or a white LED (serving as a broadband spectrum source) was used, with the spot size approximately matching the membrane diameter. The light power was modulated using a square wave signal with frequencies of 1, 10, and 100 Hz. To probe the out-of-plane deformation of the membrane, a low-power green laser was used (<1 mW, 532 nm), and the amplitude of the membrane reflectivity was detected using a photodiode. Additionally, the setup was equipped with a CCD camera, selective light filters, and low-intensity white light illumination to enable optical imaging of the membrane morphology.

### X-ray reflectivity

XRR measurements (Fig. S1, ESI†) were performed on a Bruker D8 Discover diffractometer. The moisture level was controlled using the Linkam RHGen humidity controller, which introduced air with RH between 10 and 90% into a home-built cell where the sample was placed. The humidity cell was a sealed box with 70 μm-thick Kapton tape windows, allowing for the scattering of incident X-rays from the sample and detection. The scan range of the diffraction angle $2\theta$ was between 0.1° and 4°, and the step width was 0.025°. The knife edge was placed ∼100 μm above the sample surface. Rocking curves were taken at $2\theta$ = 0.9° and allowed for determining the film critical angle from the maxima of the Yoneda wings and, thus, the film density.

### Micro-Brillouin light scattering spectroscopy

The μ-BLS experiments were carried out in the p–p backscattering geometry using a high-contrast tandem-type Fabry–Perot interferometer and a solid-state laser (Excelsior, Spectra-Physics, 532 nm). Using a microscope objective with a 10× magnification and a numerical aperture of 0.25, the incident and backscattered light were focused and collected, respectively. The laser incidence power was 0.8 mW. For observations in the ±1.7 GHz frequency range, the spectrometer mirror spacing was adjusted to 33 mm, and the scanning amplitude was 200 nm. A decreased scanning amplitude of 70 nm was applied for scattering angles lower than 32 degrees to increase the spectral resolution. All μ-BLS measurements were performed under ambient room conditions (23 °C, RH ≈ 30%).

## Author contributions

The manuscript was written with contributions from all authors. All authors have approved the final version of the manuscript. A. K. analyzed all the experimental data, carried out optical microscopy imaging, and wrote the first draft of the manuscript. A. K. and B. G. carried out μ-BLS measurements. M. W. and M. P. built the optodynamic apparatus and carried out optodynamic measurements. M. B., J. Y., T. M. A., Ch. V. S., and T. W. fabricated the samples. A. K., P. P., and P. M. carried out XRR and the low-angle rocking curve measurements. B. G. proposed, supervised, and conceived the study.

## Conflicts of interest

There are no conflicts to declare.

## Acknowledgements

A. K., M. W., M. P., and B. G. acknowledge the National Science Centre of Poland (NCN) for the OPUS grant UMO-2021/41/B/ST5/03038. P. P. and P. W. M. would like to

acknowledge the financial support from the First Team program (POIR.04.04.00-00-1DE6/16) of the Foundation for Polish Science co-financed by the European Union under the European Regional Development Fund. T. W., M. B., and C. V. S. gratefully acknowledge funding by the German Research Foundation (DFG) – project number 364549901 – TRR234 (CataLight, B04). J. Y. acknowledges funding through a Ph.D. scholarship by the Chinese Scholarship Council. C. V. S. acknowledges funding from the Sino-German mobility program M-0424.

## References

1 G. Pasparakis and M. Vamvakaki, *Polym. Chem.*, 2011, **2**, 1234.
2 M. Behl and A. Lendlein, *Mater. Today*, 2007, **10**, 20–28.
3 F. Liu and M. W. Urban, *Prog. Polym. Sci.*, 2010, **35**, 3–23.
4 S. G. Lee, D. Y. Lee, H. S. Lim, D. H. Lee, S. Lee and K. Cho, *Adv. Mater.*, 2010, **22**, 5013–5017.
5 Y. Zhou, F. Fan, Y. Liu, S. Zhao, Q. Xu, S. Wang, D. Luo and Y. Long, *Nano Energy*, 2021, **90**, 106613.
6 W. Hong, Z. Yuan and X. Chen, *Small*, 2020, **16**, 1907626.
7 X. Jiang, Y. Zheng, H. H. Chen, K. W. Leong, T. Wang and H. Mao, *Adv. Mater.*, 2010, **22**, 2556–2560.
8 F. J. Xu, Y. Zhu, F. S. Liu, J. Nie, J. Ma and W. T. Yang, *Bioconjugate Chem.*, 2010, **21**, 456–464.
9 X. Tan, P. Gao, Y. Li, P. Qi, J. Liu, R. Shen, L. Wang, N. Huang, K. Xiong, W. Tian and Q. Tu, *Bioact. Mater.*, 2021, **6**, 285–296.
10 J. Cai, J. Guo, M. Ji, W. Yang, C. Wang and S. Fu, *Colloid Polym. Sci.*, 2007, **285**, 1607–1615.
11 W. Wu, N. Mitra, E. C. Y. Yan and S. Zhou, *ACS Nano*, 2010, **4**, 4831–4839.
12 K. Matsubara, M. Watanabe and Y. Takeoka, *Angew. Chem., Int. Ed.*, 2007, **46**, 1688–1692.
13 J. Kim, S. E. Chung, S.-E. Choi, H. Lee, J. Kim and S. Kwon, *Nat. Mater.*, 2011, **10**, 747–752.
14 E. Palleau, D. Morales, M. D. Dickey and O. D. Velev, *Nat. Commun.*, 2013, **4**, 2257.
15 D. Morales, E. Palleau, M. D. Dickey and O. D. Velev, *Soft Matter*, 2014, **10**, 1337–1348.
16 M. Nandi, B. Maiti and D. Díaz Díaz, *Adv. Intell. Syst.*, 2021, **3**, 2000214.
17 H. Tian, Z. Wang, Y. Chen, J. Shao, T. Gao and S. Cai, *ACS Appl. Mater. Interfaces*, 2018, **10**, 8307–8316.
18 C. Huang, J. Lv, X. Tian, Y. Wang, Y. Yu and J. Liu, *Sci. Rep.*, 2015, **5**, 17414.
19 C. Li, A. Iscen, L. C. Palmer, G. C. Schatz and S. I. Stupp, *J. Am. Chem. Soc.*, 2020, **142**, 8447–8453.
20 E. C. Davidson, A. Kotikian, S. Li, J. Aizenberg and J. A. Lewis, *Adv. Mater.*, 2020, **32**, 1905682.
21 Y. Chen, C. Yu, X. Zhu and Q. Yu, *Dalton Trans.*, 2023, **52**, 12194–12197.
22 Z. Li, Y. Yang, Z. Wang, X. Zhang, Q. Chen, X. Qian, N. Liu, Y. Wei and Y. Ji, *J. Mater. Chem. A*, 2017, **5**, 6740–6746.
23 Y. Li, H. Zhuo, H. Chen and S. Chen, *Polymer*, 2019, **179**, 121671.
24 Y. Huang, Q. Yu, C. Su, J. Jiang, N. Chen and H. Shao, *Actuators*, 2021, **10**, 298.
25 C. Morris, B. Szczupak, A. S. Klymchenko and A. G. Ryder, *Macromolecules*, 2010, **43**, 9488–9494.
26 J. Szewczyk, D. Aguilar-Ferrer and E. Coy, *Eur. Polym. J.*, 2022, **174**, 111346.
27 V. Ball, J. Hirtzel, G. Leks, B. Frisch and I. Talon, *Macromol. Rapid Commun.*, 2023, **44**, 2200946.
28 T. Vasileiadis, T. Marchesi D'Alvise, C.-M. Saak, M. Pochylski, S. Harvey, C. V. Synatschke, J. Gapinski, G. Fytas, E. H. G. Backus, T. Weil and B. Graczykowski, *Nano Lett.*, 2022, **22**, 578–585.
29 N. Augustine, S. Putzke, A. Janke, F. Simon, A. Drechsler and C. A. Zimmerer, *ACS Appl. Mater. Interfaces*, 2022, **14**, 5921–5931.
30 H. Lee, J. Rho and P. B. Messersmith, *Adv. Mater.*, 2009, **21**, 431–434.
31 J. Saiz-Poseu, J. Mancebo-Aracil, F. Nador, F. Busqué and D. Ruiz-Molina, *Angew. Chem., Int. Ed.*, 2019, **58**, 696–714.
32 H. Lee, S. M. Dellatore, W. M. Miller and P. B. Messersmith, *Science*, 2007, **318**, 426–430.
33 J. Szewczyk, M. Ziółek, K. Siuzdak, I. Iatsunskyi, M. Pochylski, D. Aguilar-Ferrer, M. Kempiński, F. Tanos, J. Gapiński, M. Bechelany and E. Coy, *Eur. Polym. J.*, 2024, **206**, 112781.
34 D. Aguilar-Ferrer, J. Szewczyk and E. Coy, *Catal. Today*, 2022, **397–399**, 316–349.
35 J. Zhou, P. Wang, C. Wang, Y. T. Goh, Z. Fang, P. B. Messersmith and H. Duan, *ACS Nano*, 2015, **9**, 6951–6960.
36 D. Aguilar-Ferrer, T. Vasileiadis, I. Iatsunskyi, M. Ziółek, K. Żebrowska, O. Ivashchenko, P. Błaszkiewicz, B. Grześkowiak, R. Pazos, S. Moya, M. Bechelany and E. Coy, *Adv. Funct. Mater.*, 2023, **33**, 2304208.
37 J. Szewczyk, I. Iatsunskyi, P. P. Michałowski, K. Załęski, C. Lamboux, S. Sayegh, E. Makhoul, A. Cabot, X. Chang, M. Bechelany and E. Coy, *ACS Appl. Mater. Interfaces*, 2024, **16**, 10774–10784.
38 A. Petran, C. Filip, D. Bogdan, C. Zimmerer, S. Beck, T. Radu and J. Liebscher, *Langmuir*, 2023, **39**, 5610–5620.
39 P. Kowalczyk, K. Kopeć, M. Wojasiński, J. Jaroszewicz and T. Ciach, *Biomater. Adv.*, 2023, **151**, 213489.
40 K. Kopeć, R. Podgórski, T. Ciach and M. Wojasiński, *ACS Omega*, 2023, **8**, 22055–22066.
41 D. Maziukiewicz, R. Mrówczyński, S. Jurga and B. F. Grześkowiak, *Diamond Relat. Mater.*, 2022, **128**, 109308.
42 M. Massaro, M. Laura Alfieri, G. Rizzo, F. Babudri, R. Barbosa De Melo, T. Faddetta, G. Gallo, A. Napolitano, R. Sanchèz-Espejo, C. Viseras Iborra and S. Riela, *J. Colloid Interface Sci.*, 2023, **646**, 910–921.
43 B. F. Grześkowiak, D. Maziukiewicz, A. Kozłowska, A. Kertmen, E. Coy and R. Mrówczyński, *Int. J. Mol. Sci.*, 2021, **22**, 738.

 

44 Y. Liu, K. Ai and L. Lu, *Chem. Rev.*, 2014, **114**, 5057–5115.
45 Y. Liu, K. Ai, J. Liu, M. Deng, Y. He and L. Lu, *Adv. Mater.*, 2013, **25**, 1353–1359.
46 C.-T. Chen, C. Chuang, J. Cao, V. Ball, D. Ruch and M. J. Buehler, *Nat. Commun.*, 2014, **5**, 3859.
47 K. G. Malollari, P. Delparastan, C. Sobek, S. J. Vachhani, T. D. Fink, R. H. Zha and P. B. Messersmith, *ACS Appl. Mater. Interfaces*, 2019, **11**, 43599–43607.
48 B. Roy, S. A. Khan, S. Chakraborty and P. C. Nath, in *Polymeric Nanocomposite Materials for Sensor Applications*, ed. J. Parameswaranpillai and S. Ganguly, Woodhead Publishing, 2023, pp. 267–293.
49 M. Gu and T. J. Echtermeyer, *Small*, 2024, 2311001.
50 J. Yu, T. Marchesi D'Alvise, I. Harley, A. Krysztofik, I. Lieberwirth, P. Pula, P. W. Majewski, B. Graczykowski, J. Hunger, K. Landfester, C. V. Synatschke and T. Weil, *Adv. Mater.*, 2024, 2401137, DOI: **10.1002/adma.202401137**.
51 H. J. Nam, J. Cha, S. H. Lee, W. J. Yoo and D.-Y. Jung, *Chem. Commun.*, 2014, **50**, 1458–1461.
52 Y. Jiang, Y. Lan, X. Yin, H. Yang, J. Cui, T. Zhu and G. Li, *J. Mater. Chem. C*, 2013, **1**, 6136–6144.
53 P. Zuo, Y. Li, A. Wang, R. Tan, Y. Liu, X. Liang, F. Sheng, G. Tang, L. Ge, L. Wu, Q. Song, N. B. McKeown, Z. Yang and T. Xu, *Angew. Chem., Int. Ed.*, 2020, **59**, 9564–9573.
54 C. Ye, R. Tan, A. Wang, J. Chen, B. Comesaña Gándara, C. Breakwell, A. Alvarez-Fernandez, Z. Fan, J. Weng, C. G. Bezzu, S. Guldin, N. P. Brandon, A. R. Kucernak, K. E. Jelfs, N. B. McKeown and Q. Song, *Angew. Chem., Int. Ed.*, 2022, **61**, e202207580.
55 M. Kucińska, D. Nowak, P. Zawadzki, T. Kazimierczak, P. Kula, R. Atraszkiewicz, A. Jeziorna, Ł. Kołodziejczyk, P. Kowalczyk and K. Dybowski, *Arch. Metall. Mater.*, 2018, **63**(3), 1379–1383.
56 X. Zhang, Q. Huang, F. Deng, H. Huang, Q. Wan, M. Liu and Y. Wei, *Appl. Mater. Today*, 2017, **7**, 222–238.
57 Y. Kim, E. Coy, H. Kim, R. Mrówczyński, P. Torruella, D.-W. Jeong, K. S. Choi, J. H. Jang, M. Y. Song, D.-J. Jang, F. Peiro, S. Jurga and H. J. Kim, *Appl. Catal., B*, 2021, **280**, 119423.
58 O. Malinkiewicz, A. Yella, Y. H. Lee, G. M. Espallargas, M. Graetzel, M. K. Nazeeruddin and H. J. Bolink, *Nat. Photonics*, 2014, **8**, 128–132.
59 K. Kopeć, A. Ryżko, R. Major, H. Plutecka, J. WiÈ©cek, G. Pikus, J. W. Trzciński, A. Kalinowska and T. Ciach, *ACS Omega*, 2022, **7**, 39234–39249.
60 T. Marchesi D'Alvise, S. Harvey, L. Hueske, J. Szelwicka, L. Veith, T. P. J. Knowles, D. Kubiczek, C. Flaig, F. Port, K. Gottschalk, F. Rosenau, B. Graczykowski, G. Fytas, F. S. Ruggeri, K. Wunderlich and T. Weil, *Adv. Funct. Mater.*, 2020, **30**, 2000378.
61 T. Marchesi D'Alvise, S. Sunder, R. Hasler, J. Moser, W. Knoll, C. V. Synatschke, S. Harvey and T. Weil, *Macromol. Rapid Commun.*, 2023, **44**, 2200332.
62 B. Graczykowski, M. Sledzinska, M. Placidi, D. Saleta Reig, M. Kasprzak, F. Alzina and C. M. Sotomayor Torres, *Nano Lett.*, 2017, **17**, 7647–7651.
63 J. Szewczyk, V. Babacic, A. Krysztofik, O. Ivashchenko, M. Pochylski, R. Pietrzak, J. Gapiński, B. Graczykowski, M. Bechelany and E. Coy, *ACS Appl. Mater. Interfaces*, 2023, **15**, 36922–36935.
64 N. Kucuk, M. Cakir and N. A. Isitman, *Radiat. Prot. Dosim.*, 2013, **153**, 127–134.
65 N. Gomopoulos, W. Cheng, M. Efremov, P. F. Nealey and G. Fytas, *Macromolecules*, 2009, **42**, 7164–7167.
66 R. K. Bay, K. Zarybnicka, J. Jančář and A. J. Crosby, *ACS Appl. Polym. Mater.*, 2020, **2**, 2220–2227.
67 R. K. Bay and A. J. Crosby, *ACS Macro Lett.*, 2019, **8**, 1080–1085.
68 G. Wang, F. Najafi, K. Ho, M. Hamidinejad, T. Cui, G. C. Walker, C. V. Singh and T. Filleter, *Macromolecules*, 2022, **55**, 1248–1259.
69 N. Lindahl, D. Midtvedt, J. Svensson, O. A. Nerushev, N. Lindvall, A. Isacsson and E. E. B. Campbell, *Nano Lett.*, 2012, **12**, 3526–3531.
70 M. Ji, N. Jiang, J. Chang and J. Sun, *Adv. Funct. Mater.*, 2014, **24**, 5412–5419.
71 C. Li, Y. Xue, M. Han, L. C. Palmer, J. A. Rogers, Y. Huang and S. I. Stupp, *Matter*, 2021, **4**, 1377–1390.
72 J.-H. Yun, C. Li, S. Kim and M. Cho, *J. Phys. Chem. C*, 2018, **122**, 6310–6317.